A&A 600, L3 (2017)
DOI: 10.1051/0004-6361/201630359

Astronomy & Astrophysics

Letter to the Editor

Planck's dusty GEMS

III. A massive lensing galaxy with a bottom-heavy stellar initial mass function at $z = 1.5$⋆

R. Cañameras[1], N. P. H. Nesvadba[1], R. Kneissl[2,3], M. Limousin[4], R. Gavazzi[5], D. Scott[6], H. Dole[1], B. Frye[7], S. Koenig[8], E. Le Floc'h[9], and I. Oteo[10,11]

(Affiliations can be found after the references)

Received 26 December 2016 / Accepted 15 February 2017

ABSTRACT

We study the properties of the foreground galaxy of the Ruby, the brightest gravitationally lensed high-redshift galaxy on the sub-millimeter sky as probed by the *Planck* satellite, and part of our sample of *Planck*'s dusty GEMS. The Ruby consists of an Einstein ring of 1.4″ diameter at $z = 3.005$ observed with ALMA at 0.1″ resolution, centered on a faint, red, massive lensing galaxy seen with HST/WFC3, which itself has an exceptionally high redshift, $z = 1.525 \pm 0.001$, as confirmed with VLT/X-shooter spectroscopy. Here we focus on the properties of the lens and the lensing model obtained with LENSTOOL. The rest-frame optical morphology of this system is strongly dominated by the lens, while the Ruby itself is highly obscured, and contributes less than 10% to the photometry out to the K band. The foreground galaxy has a lensing mass of $(3.70 \pm 0.35) \times 10^{11}\,M_{\odot}$. Magnification factors are between 7 and 38 for individual clumps forming two image families along the Einstein ring. We present a decomposition of the foreground and background sources in the WFC3 images, and stellar population synthesis modeling with a range of star-formation histories for Chabrier and Salpeter initial mass functions (IMFs). Only the stellar mass range obtained with the latter agrees well with the lensing mass. This is consistent with the bottom-heavy IMFs of massive high-redshift galaxies expected from detailed studies of the stellar masses and mass profiles of their low-redshift descendants, and from models of turbulent gas fragmentation. This may be the first direct constraint on the IMF in a lens at $z = 1.5$, which is not a cluster central galaxy.

Key words. galaxies: high-redshift – galaxies: evolution – galaxies: star formation – galaxies: stellar content – infrared: galaxies – submillimeter: galaxies

1. Introduction

Dark-matter halo mass is a major driver of galaxy evolution (e.g., Peng et al. 2010), but such halo mass is very challenging to measure at high redshift. Only in a few exceptional cases is the stellar continuum bright enough for absorption-line measurements (e.g., van de Sande et al. 2013). Dynamical masses measured from gas motions are affected by inclination and beam-smearing effects and, potentially, the kinetic energy injected by feedback or accretion and merger events. Moreover, the degeneracy between age, extinction, and metallicity limits the accuracy of stellar masses estimated from broadband colors, which is further reduced by the largely unknown shape of the initial mass function (IMF). Fossil evidence in nearby massive early-type galaxies suggests bottom-heavy IMFs (e.g., Conroy et al. 2013), whereas galaxy evolution models favor top-heavy IMFs (e.g., Lacey et al. 2016). The lack of direct constraints on the IMF not only limits the accuracy of stellar mass estimates in high-redshift galaxies (e.g., Conroy et al. 2009), but also hides from us important information on the regulation mechanisms of star formation (e.g., Chabrier et al. 2014).

The size of the Einstein ring around a massive galaxy only depends on the projected mass along the line of sight. Gravitational lensing therefore offers an opportunity to measure directly galaxy masses that are unaffected by the detailed baryonic properties of the lens. The number of known strong lensing galaxies during the major phase of galaxy evolution at $z \geq 1$ is however very small. We are only aware of two such galaxies at $z \geq 1.5$: a massive galaxy at $z = 1.62$ found by Wong et al. (2014), which is a brightest cluster galaxy and might therefore have an atypical formation history and mass profile; and the galaxy found by van der Wel et al. (2013) at $z = 1.53$, which unfortunately has no bright line emission and only a photometric redshift.

Here we characterize a new lensing galaxy at $z = 1.525$, which is magnifying the brightest high-redshift galaxy in the Planck Catalogue of Compact Sources (Planck Collaboration XXVIII 2014; Planck Collaboration Int. XXVII 2015), a maximally starbursting galaxy at $z = 3.0$ (the "Ruby"; Cañameras et al. 2017, C17 hereafter). The Ruby is part of our follow up of the "Planck's dusty GEMS" (gravitationally enhanced submillimeter sources) sample, which includes the brightest gravitationally lensed high-redshift galaxies discovered with Planck on the roughly 50% of sky not dominated by Galactic foregrounds (Planck Collaboration Int. XXVII 2015; Cañameras et al. 2015; Nesvadba et al. 2016). We focus on the optical and near-infrared properties, including the spectroscopic redshift of the foreground source and the lensing model, and discuss the stellar mass and mass-to-light ratio, which favor a bottom-heavy stellar IMF. The detailed properties of the background source are discussed in C17.

We adopt the flat ΛCDM cosmology from Planck Collaboration XVI (2014) with $H_0 = 68\,\mathrm{km\,s^{-1}\,Mpc^{-1}}$, $\Omega_\mathrm{m} = 0.31$, and $\Omega_\Lambda = 1 - \Omega_\mathrm{m}$. At $z = 3.005$ this implies a luminosity distance, $D_\mathrm{L} = 26.0\,\mathrm{Gpc}$, and a projected physical scale of

⋆ Based on ALMA data obtained with program 2015.1.01518S and VLT data obtained with programs 291.A-5014 and 295.A-5017.

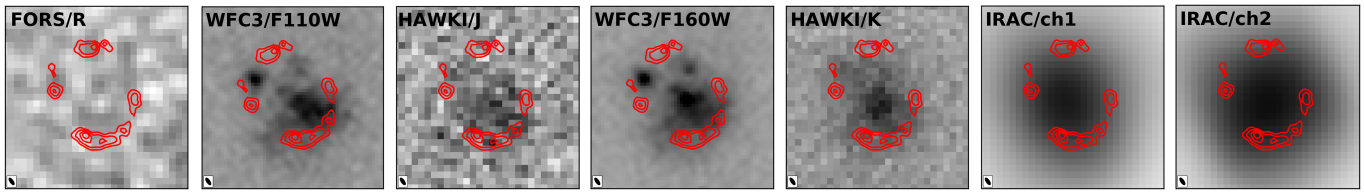

Fig. 1. *Left to right*: three arcsecond wide postage stamps of the Ruby in the *R*, *F110W*, *J*, *F160W*, *K*, 3.6-μm, and 4.5-μm bands. Contours show the CO morphology from C17 taken with $0.14'' \times 0.06''$ beam size (lower left corner of each panel); they start at 3σ, and increase in steps of 3σ.

7.9 kpc arcsec^{-1}. At $z = 1.525$, $D_{\rm L} = 11.3$ Gpc, and the projected scale is 8.6 kpc arcsec^{-1}. All magnitudes are in the AB system.

2. Morphology in the near-infrared and millimeter

We obtained optical and near-IR imaging of the Ruby on 8 May 2013, using FORS2 through the *V*-, *R*-, and *I*-band filters at $1''$ seeing with exposure times of 23, 9, and 13 min and limiting depths of 27.4, 26.9, and 26.2 mag, respectively. With HAWK-I we observed the Ruby on 12 May 2013 with $0.4''$ seeing, reaching limiting magnitudes of 24.2, and 23.6 mag in the *J* and *K* band, respectively, in 26 and 30 min of total observing time.

We used the ESO pipeline to align the images from the two detectors of FORS2 and to reduce the images in the standard way, by subtracting bias or dark frames and dividing by the flat-field. We used SWARP and SCAMP (Bertin 2010a,b) to align individual frames relative to each other and within the World Coordinate System, as probed by the 7th data release of the SDSS, and to construct the final images. Positional mismatches between bands suggest an rms uncertainty of at most $0.1''$ in the final images. Optical images were flux calibrated using the zero points on the ESO website and the NIR bands were calibrated relative to 2MASS. We also ensured that the relative photometry is robust between bands using the blackbody spectral energy distribution of stars within all bands.

We used high-resolution observations of CO $J = 4 \rightarrow 3$ and dust continuum obtained with ALMA in band 3 (program 2015.1.01518S, P.I. Nesvadba) and with the Wide-Field Camera 3 on the *Hubble* Space Telescope in the *F110W* and *F160W* bands (program 14223, P.I. Frye). These data will be discussed in detail in forthcoming papers (C17; Frye et al., in prep.).

The morphology of the Ruby in the optical, near-infrared, and millimeter is shown in Fig. 1. The optical and near-infrared bands are dominated by a faint, red source in the center of a nearly complete Einstein ring with $1.4''$ diameter, which can only be seen at long wavelengths. With ALMA in CO($4 \rightarrow 3$) we detect six clumps along this ring (Fig. 3), which we associate with two systems of multiple images, as described below.

3. Spectroscopic redshift with VLT/X-shooter

We obtained VLT/X-shooter spectroscopy from 390 to 2500 nm through DDT program 295.A-5017 (P.I.: N. Nesvadba) with a total observing time of 4 h under good and stable conditions and seeing $<1''$. Slit widths were $1.2''$ in the two optical and $1.3''$ in the NIR arm. For completeness, earlier X-shooter data taken in June 2015 and contaminated by a bright foreground source were discarded. Data were reduced with the ESO X-shooter pipeline in the standard way (Modigliani et al. 2010).

We find Hα at $(1.6566 \pm 0.0005)\,\mu$m and the [N II]$\lambda\lambda$6548, 6583 doublet at $(1.65281 \pm 0.0005)\,\mu$m and $(1.6617 \pm 0.0005)\,\mu$m, respectively, at a common redshift $z = 1.525 \pm 0.001$ (Fig. 2). Full width at half maximum (FWHM) line widths are (206 ± 20) km s^{-1} and (306 ± 41) km s^{-1} for Hα, and [N II], respectively. No other line is seen between 0.3 and 2.4 μm. Non-detections of [O III]$\lambda\lambda$4959, 5007, Hβ, and [O II]λ3728 are consistent with high metallicity (e.g., Nesvadba et al. 2007) or extinction; however, the high [N II]λ6583/Hα ratio of 0.69 ± 0.1 suggests the presence of a faint AGN (Kewley et al. 2013), which precludes using [N II]/Hα as a metallicity indicator.

4. Lens modeling and source reconstruction

We use LENSTOOL (Jullo et al. 2007) to model the strong gravitational lensing toward the Ruby. LENSTOOL is a publicly available Bayesian lens modeling code, which approximates the foreground mass distribution through a range of models. We use the truncated pseudo-isothermal elliptical mass density profiles (PIEMD; Elíasdóttir et al. 2007). Briefly summarized, LENSTOOL uses the number of arclets in the image plane, their association with image systems of the same regions in the source plane, and their positions relative to the caustic line as input parameters to constrain the elliptical lens potential and magnification map (Kneib 1993). The modeled parameter space is sampled with a Markov chain Monte Carlo (MCMC) approach, where the posterior likelihood distribution quantifies the parameter uncertainties.

The near-circular shape of the Einstein ring shows that the faint source in the center of the ring at $z = 1.525$ is the main deflector. A bright, S0 galaxy at $z = 0.13$ is at around $30''$ distance. The LENSTOOL models with and without this galaxy show that it has no significant impact on the shear and magnification.

We measure the peak position of individual lensed arclets in the ALMA CO($4 \rightarrow 3$) flux map at $0.14'' \times 0.06''$ beam size. The orientation of the velocity gradients indicate the image parity in the lens plane (see also Riechers et al. 2008; ALMA Partnership et al. 2015), but since the velocities partially overlap, identifying image families unambiguously remains difficult. We therefore tested 10 plausible associations of individual arclets into image families and adopted the single model that converges and places all images at positions matching those observed. This results in two image systems with two and four images, respectively, and is a configuration that is also commonly found in other strong lensing systems (e.g., Gavazzi et al. 2008; Tu et al. 2009; Limousin et al. 2009; Bayliss et al. 2011). We fitted the centroid position in right ascension, ΔRA, and declination, ΔDec, the velocity dispersion of the PIEMD, $\sigma_{\rm PIEMD}$, as well as its ellipticity, ϵ, and position angle, PA (see also Limousin et al. 2013; Bonamigo et al. 2015). The core and cut-off radii are poorly constrained with an Einstein ring of about 6.2 kpc at $z = 1.525$. We therefore choose to fix $r_{\rm core} = 0.15$ kpc (e.g., Limousin et al. 2007; Richard et al. 2014), and $r_{\rm cut} = 100$ kpc (e.g., Brainerd et al. 1996), which are typical values for isolated galaxies. Varying these values within our observational constraints changes the mass estimate by $<10\%$.

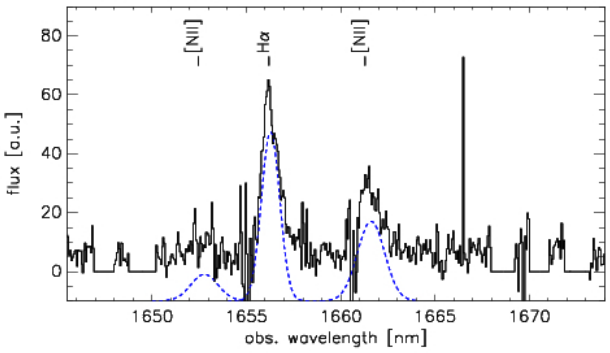

Fig. 2. VLT/X-shooter spectrum of Hα and [N II]$\lambda\lambda$6548, 6583 in the lens at $z = 1.525 \pm 0.001$. Blue lines show Gaussian line fits. Bright night-sky line residuals are clipped.

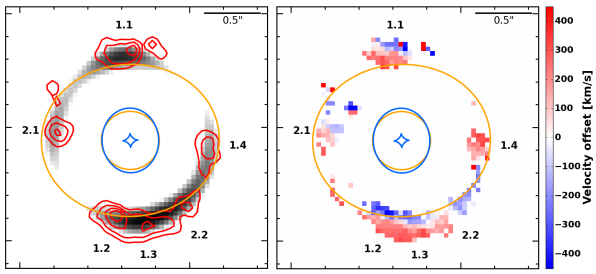

Fig. 3. *Left*: reconstructed (grayscale) and observed (contours) CO(4 → 3) surface brightness observed with ALMA. *Right*: CO(4 → 3) velocity map of the Ruby. We label the two sets of multiple images; we show the tangential and radial critical curves at $z = 1.525$ and caustic lines at $z = 3.005$ as orange and blue lines, respectively.

Table 1. Gravitational magnification factors.

ID	1.1	1.2	1.3	1.4	2.1	2.2
$\mu_{\rm clump}$	22 ± 2	41 ± 5	30 ± 3	17 ± 3	11 ± 2	42 ± 6
$\mu_{\rm peak}$	11 ± 1	27 ± 3	11 ± 1	13 ± 2	7 ± 1	22 ± 2

Notes. $\mu_{\rm clump}$ lists luminosity-weighted average magnifications in each image. $\mu_{\rm peak}$ is the magnification at the peak.

With this approach, we find that the data are best fitted with a potential of ellipticity $\epsilon = 0.113$, position angle PA $= +2.7°$ (measured from north to east), and velocity dispersion $\sigma_{\rm PIEMD} = 260.6\,{\rm km\,s^{-1}}$. The reconstructed center of mass is offset by $\Delta{\rm RA} = -0.054''$ and $\Delta{\rm Dec} = +0.100''$, from the reference position at $\alpha = 163.47138°$ and $\delta = 5.938551°$, respectively. Figure 3 illustrates that the source falls near the tangential critical line and that the data are well fitted by our model. The rms of the offsets between observed and reconstructed images is $0.07''$, which is about half the ALMA beam. Varying the image positions within this beam does not significantly alter the results. The best-fitting PIEMD is offset by $\lesssim 0.1''$ from the galaxy center in the WFC3/F160W image. At low redshift, we would not expect such offsets (Koopmans et al. 2006); but at $z = 1.5$, this offset could be from variations in extinction or star formation history, if not astrometric uncertainties.

We compute a mean magnification map and uncertainties for each pixel using 4000 MCMC iterations. Table 1 lists the magnification factors at the peak of each image and the range in magnification in each spatially resolved (C17) image. In small regions around caustics factors are up to 60–100. Magnification factors are consistent with flux ratios.

The source-plane morphology of each image is reconstructed by ray tracing the image pixel by pixel through the modeled gravitational potential ("cleanlens"; Sharon et al. 2012). We use again 4000 MCMC iterations to determine the uncertainties on the source-plane positions. We obtain matching positions for each component of the two image systems, near the diamond-shaped caustic, offset by 470 pc from each other in the source plane. Their intrinsic properties are further discussed in C17.

5. A massive lensing galaxy at $z = 1.5$

Gravitational lensing provides the most accurate estimates of the integrated mass within the Einstein radius. Following Limousin et al. (2005), we derive the mass of the deflector of the Ruby from the mean radial profile of the PIEMD and the parameters listed in Sect. 4, finding an enclosed mass of $M_{\rm aper}(\theta_{\rm E}) = (3.70 \pm 0.35) \times 10^{11}\,M_\odot$ that is accurate to about 10%, within the Einstein ring, $\theta_{\rm E} = 0.72'' \pm 0.06''$, corresponding to (6.2 ± 0.5) kpc at $z = 1.525$.

We can estimate a stellar mass of the deflector from our optical and NIR photometry, after constraining the possible contamination from the Ruby. To do this we calculate an azimuthally averaged surface-brightness profile from our highest resolution image, *WFC3/F160W* (Fig. 1), after masking a ring with a thickness of twice the PSF ($0.18''$) around the caustic line (red band in Fig. 4) to avoid contamination from the Ruby. Figure 4 shows that the deflector is well fit with a near exponential profile that has a Sersic index of 1.15 ± 0.29 and a half-light radius of $0.75'' \pm 0.23''$, or (6.5 ± 1.9) kpc at $z = 1.525$. We do not see strong residuals in the inner region, but observe a faint excess at radii near the caustic line, corresponding to about 15% of the total flux. The same profile is also a good match to the WFC3/*F110W* image (Fig. 4). Convolving this profile with the HAWK-I *K*-band point spread function suggests that the contamination from the Ruby in this band is also very mild, indicating that the optical and NIR photometry can be used to constrain the star formation history and stellar population in the deflector.

We use the population synthesis code of Bruzual & Charlot (2003), with solar metallicity, as is common for massive galaxies, a Chabrier (2003) IMF, and the Calzetti et al. (1994) extinction law to fit the photometry of the deflector in the *I*, *F110W*, *F160W*, and *K* band with an exponentially declining star formation history with $\tau = 20$–200 Myr, and ages between 1 and 3 Gyr and $A_V = 1$–2 mag. Stellar absorption line spectra in massive early-type galaxies at low and high redshift with enhanced abundance ratios of α elements relative to iron suggest bursty star formation histories for massive galaxies like the one studied here (Thomas et al. 2005; Kriek et al. 2016). Younger unobscured starbursts are ruled out by the absence of a blue continuum and older ages by the age of the Universe at $z = 1.5$. A young, dusty burst is ruled out by the upper limit on the dust continuum at 3 mm from our ALMA data (C17) of 0.14 mJy rms, implying star formation rates <120–$140\,M_\odot\,{\rm yr^{-1}}$. Our best-fitting model that does not overestimate the emission in the optical is 3 Gyr old with $A_v = 1.5$ mag. Overall, models within the above range of star formation histories fitting our SED with $\chi^2 < 5$ result in stellar masses of 2–$2.5 \times 10^{11}\,M_\odot$. When using a Salpeter (1955) IMF instead, we find masses that are greater by a factor of 1.7. These estimates do not depend strongly on metallicity. For example, when using models with 2.5 times the solar metallicity, we found stellar masses that were lower by 12–15%.

In Fig. 5 we show the optical-to-NIR photometry of the Ruby and our best-fit SED of the lens, matched to the ground-based

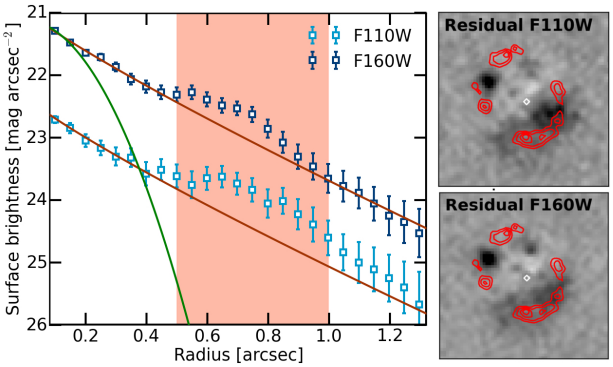

Fig. 4. *Left*: azimuthally-averaged surface brightness profiles in the *WFC3/F160W* and *110W* bands. The PSF is shown in green. The red band indicates radii near the critical line, where the Ruby might contribute and where an excess is seen compared to the Sersic profile (red line) fitted to the inner 0.5″ in the *F160W* band. The fit to the *F110W* band was simply scaled to the central surface brightness. These regions are also seen in the residual images (*right*) after subtracting the model.

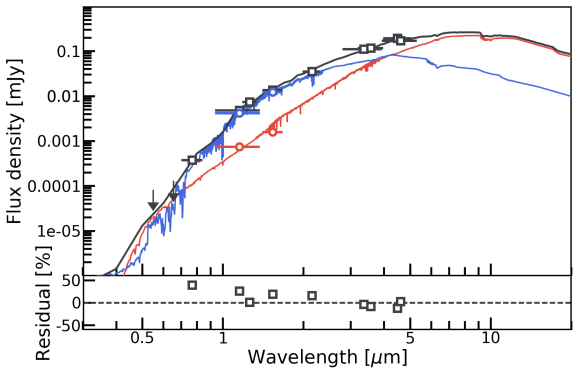

Fig. 5. Spectral energy distribution of the deflector (blue) and Ruby (red). The combined SED is shown in black. Black squares show the total photometry, while blue and red dots are the resolved photometry of the foreground galaxy and the Ruby in the *F110W* and *F160W* images, respectively.

photometry from the V to K bands. In the IRAC 3.6-μm and 4.5-μm bands the contribution from the Ruby is no longer negligible (Fig. 5). The combined photometry for both sources is well matched, when adopting a young burst with $\tau = 50$ Myr, 10 Myr age, and $A_V = 4.5$ mag for the Ruby.

6. Evidence for a bottom-heavy IMF

The mass profiles of massive galaxies at low redshift suggest that dark matter contributes at most 10% to the total mass out to 6–7 kpc (Auger et al. 2010; Conroy et al. 2013) and probably less in our source at $z = 1.5$, owing to gradual dark-matter assembly (Macciò et al. 2008). The non-detection of the dust continuum with ALMA (C17) also rules out masses of cold molecular and atomic gas above on the order of 10^9 $M_\odot$ (1% of $M_{\rm lens}$), for a simple scaling with the range of gas-to-dust ratios between 40 and 100, as measured by C15. This suggests $M_{\rm stellar} \simeq M_{\rm lens}$, which is the case for a Salpeter IMF, whereas a Chabrier IMF underpredicts the lensing mass by about a factor of 2. Flux near the Einstein ring contributes only 15% to the total flux in the WFC3 images, and therefore does not change our result. We also ruled out the IMFs with average mass-to-light ratios that are much greater than Salpeter, 0.4–1.5 $M_\odot/L_\odot$ in the rest-frame V band, which would produce masses greater than the lensing mass.

The difference between the two IMFs is the slope at stellar masses <1 $M_\odot$, where Chabrier (2003) predict a shallower slope than the single slope of $\alpha = -2.35$ adopted by Salpeter (1955), and hence more bottom-light IMFs. Such low-mass stars are difficult to observe directly. However, the best estimates currently available, including those based on direct spectral tracers of low-mass stars, favor bottom-heavy IMFs consistent with Salpeter or even steeper slopes (Auger et al. 2010; Conroy et al. 2013; Sonnenfeld et al. 2017; van Dokkum et al. 2017), which are also consistent with our results. These IMFs should scale with galaxy mass, but not with redshift (Sonnenfeld et al. 2017); this is consistent with mainly passively evolving stellar populations since redshifts $z = 1$–2.

The low-mass end of the IMF in high-redshift galaxies is a sensitive probe of feedback processes in massive starburst galaxies. For example, Larson (2005) finds that increased Jeans masses in dense gas could make the IMF more top-heavy, whereas Chabrier et al. (2014) argue that turbulent gas fragmentation should produce bottom-heavy IMFs similar, or even steeper than Salpeter. Our result favors these bottom-heavy IMFs, and thus exacerbates the long-standing difficulty of semi-analytic galaxy evolution models to match the predicted upper end of the galaxy mass function and number of submillimeter galaxies with observations without imposing a top-heavy IMF (Lacey et al. 2016). It will therefore be very interesting to see whether our results are representative of the overall population of massive high-z galaxies, as more massive, strong lensing galaxies become known at these redshifts.

Acknowledgements. We thank the referee for comments that helped improve the paper, the ESO Director General for granting DDT, and the staff at Paranal, ALMA, and NASA for carrying out the observations. R.C. would like to thank C. Grillo for helpful discussions. M.L. acknowledges CNRS and CNES for support. O.I. acknowledges support from ERC program 321302, COSMICISM. This paper makes use of ALMA data ADS/JAO.ALMA#2015.1.01518.S.

References

ALMA Partnership, Vlahakis, C., Hunter, T. R., et al. 2015, ApJ, 808, L4
Auger, M. W., Treu, T., Bolton, A. S., et al. 2010, ApJ, 724, 511
Bayliss, M. B., Hennawi, J. F., Gladders, M. D., et al. 2011, ApJS, 193, 8
Bertin, E. 2010a, SCAMP, Astrophysics Source Code Library [record ascl:1010.063]
Bertin, E. 2010b, SWarp, Astrophysics Source Code Library [record ascl:1010.068]
Bonamigo, M., Despali, G., Limousin, M., et al. 2015, MNRAS, 449, 3171
Brainerd, T. G., Blandford, R. D., & Smail, I. 1996, ApJ, 466, 623
Bruzual, G., & Charlot, S. 2003, MNRAS, 344, 1000
Calzetti, D., Kinney, A. L., & Storchi-Bergmann, T. 1994, ApJ, 429, 582
Cañameras, R., Nesvadba, N. P. H., Guery, D., et al. 2015, A&A, 581, A105
Cañameras, R., Nesvadba, N. P. H., Kneissl, R., et al. 2017, A&A, submitted
Chabrier, G. 2003, PASP, 115, 763
Chabrier, G., Hennebelle, P., & Charlot, S. 2014, ApJ, 796, 75
Conroy, C., Gunn, J. E., & White, M. 2009, ApJ, 699, 486
Conroy, C., Dutton, A. A., Graves, Mendel, J. T., & van Dokkum, P. G. 2013, ApJ, 776, L26
Elíasdóttir, Á., Limousin, M., Richard, J., et al. 2007, ArXiv e-prints [arXiv:0710.5636]
Gavazzi, R., Treu, T., Koopmans, L. V. E., et al. 2008, ApJ, 677, 1046
Jullo, E., Kneib, J.-P., Limousin, M., et al. 2007, New J. Phys., 9, 447
Kewley, L. J., Dopita, M. A., Leitherer, C., et al. 2013, ApJ, 774, 100
Kneib, J.-P. 1993, Ph.D. Thesis, Université Paul Sabatier, Toulouse, France
Koopmans, L. V. E., Treu, T., Bolton, A. S., Burles, S., & Moustakas, L. A. 2006, ApJ, 649, 599
Kriek, M., Conroy, C., van Dokkum, P. G., et al. 2016, Nature, 540, 248
Lacey, C. G., Baugh, C. M., Frenk, C. S., et al. 2016, MNRAS, 462, 3854
Larson, R. B. 2005, MNRAS, 359, 211
Limousin, M., Kneib, J.-P., & Natarajan, P. 2005, MNRAS, 356, 309
Limousin, M., Cabanac, R., Gavazzi, R., et al. 2009, A&A, 502, 445
Limousin, M., Morandi, A., Sereno, M., et al. 2013, Space Sci. Rev., 177, 155

Limousin, M., Richard, J., Jullo, E., et al. 2007, ApJ, 668, 643
Macciò, A. V., Dutton, A. A., & van den Bosch, F. C. 2008, MNRAS, 391, 1940
Modigliani, A., Goldoni, P., Royer, F., et al. 2010, in SPIE, 7737, 28
Nesvadba, N. P. H., Lehnert, M. D., Genzel, R., et al. 2007, ApJ, 657, 725
Nesvadba, N., Kneissl, R., Cañameras, R., et al. 2016, A&A, 593, L2
Peng, Y.-j., Lilly, S. J., Kovač, K., et al. 2010, ApJ, 721, 193
Planck Collaboration XVI. 2014, A&A, 571, A16
Planck Collaboration XXVIII. 2014, A&A, 571, A28
Planck Collaboration Int. XXVII. 2015, A&A, 582, A30
Richard, J., Jauzac, M., Limousin, M., et al. 2014, MNRAS, 444, 268
Riechers, D. A., Walter, F., Brewer, B. J., et al. 2008, ApJ, 686, 851
Salpeter, E. E. 1955, ApJ, 121, 161
Sharon, K., Gladders, M. D., Rigby, J. R., et al. 2012, ApJ, 746, 161
Sonnenfeld, A., Nipoti, C., & Treu, T. 2017, MNRAS, 465, 2397
Thomas, D., Maraston, C., Bender, R., et al. 2005, ApJ, 621, 673
Tu, H., Gavazzi, R., Limousin, M., et al. 2009, A&A, 501, 475
van de Sande, J., Kriek, M., Franx, M., et al. 2013, ApJ, 771, 85
van der Wel, A., van de Ven, G., Maseda, M., et al. 2013, ApJ, 777, L17
van Dokkum, P., et al. 2017, ApJ, submitted [arXiv:1611.09859]
Wong, K. C., Tran, K.-V. H., Suyu, S. H., et al. 2014, ApJ, 789, L31

[1] Institut d'Astrophysique Spatiale, CNRS, Univ. Paris-Sud, Université Paris-Saday, Bât. 121, 91405 Orsay Cedex, France
e-mail: raoul.canameras@ias.u-psud.fr

[2] European Southern Observatory, ESO Vitacura, Alonso de Cordova 3107, Vitacura, Casilla 19001, Santiago, Chile
[3] Atacama Large Millimeter/submillimeter Array, ALMA Santiago Central Offices, Alonso de Cordova 3107, Vitacura, Casilla 763-0355, Santiago, Chile
[4] Aix-Marseille Université, CNRS, LAM, Laboratoire d'Astrophysique de Marseille, Marseille, France
[5] Institut d'Astrophysique de Paris, 75014 Paris, UPMC Univ. Paris 6, UMR 7095, France
[6] Department of Physics and Astronomy, University of British Columbia, 6224 Agricultural Road, Vancouver, 6658 British Columbia, Canada
[7] Steward Observatory, University of Arizona, Tucson, AZ 85721, USA
[8] Chalmers University of Technology, Onsala Space Observatory, Onsala, Sweden
[9] Laboratoire AIM, CEA/DSM/IRFU, CNRS, Université Paris-Diderot, Bât. 709, 91191 Gif-sur-Yvette, France
[10] Institute for Astronomy, University of Edinburgh, Royal Observatory, Blackford Hill, Edinburgh, EH9 3HJ, UK
[11] European Southern Observatory, Karl-Schwarzschild-Strasse 2, 85748 Garching, Germany